

## ASYMPTOTIC ANALYSIS FOR FIBER DRAWING PROCESSES\*

NIAL HANEVY<sup>†</sup> AND DOIREANN O'KIELY<sup>‡</sup>

**Abstract.** In fiber drawing, axial tension is applied to long, thin viscous threads to increase their length and consequently reduce their cross-sectional area. This process is used to manufacture rods and threads of glass and polymer such as optical fibers and filaments for textiles. Drawing is described mathematically using the Trouton model for extensional flow in a long, narrow cylinder. This leading-order description gives simple expressions for fiber radius and one-dimensional axial velocity in the long, slender limit. In this paper we determine the next-order corrections, showing that they can be an order of magnitude larger than previously assumed.

**Key words.** viscous flow, Trouton model, asymptotic analysis

**MSC codes.** 68Q25, 68R10, 68U05

**DOI.** 10.1137/22M1470074

**1. Introduction.** Drawing is an umbrella term for a family of manufacturing processes in which threads, sheets, and tubes of viscous or viscoelastic material are elongated. These processes are used in the manufacture of optical fibers [10, 29], filaments for textiles [18, 5], smartphone screens [20, 21, 22], and medical vials [11, 12, 13]. The most common drawing process is fiber drawing. Here, a thread of material continually enters a stretching zone with a given radius and velocity. It is accelerated along the stretching zone, usually by rollers at the end of the stretching zone, which draw the thread away at a fixed velocity. This acceleration leads to a reduction in the thread radius, enabling the production of fiber-optic cables and polymer threads with diameters typically in the range 10–100  $\mu\text{m}$  [29, 5]. Many variations of the process exist: in magnetospinning, tension is applied to threads of a fluid containing magnetic nanoparticles by a rotating magnet [30], while tubes and microstructured optical fibers are manufactured by drawing fibers with internal holes, with pressure often used to maintain and control the hole size [8, 11].

A simple conservation-of-mass argument can be used to quantify the relationship between the velocity of a drawn fiber and its radius. For any fiber-drawing process operating in steady state, the flux of material in and out of the system must match, so if the cross-sectionally averaged axial velocity increases by a factor  $D$ , the cross-sectional area must decrease by a factor  $1/D$ . For a circular fiber with no internal holes, the radius must therefore decrease by a factor  $1/\sqrt{D}$ . The force required to attain this acceleration and the velocity profile along the stretching zone vary between systems and can be predicted using mathematical modeling. The fluid flow in fiber drawing is typically treated as a purely viscous flow and is well-approximated by the one-dimensional *Trouton model* [31], with an axial velocity that is approximately uniform across the fiber radius. This model can be derived by exploiting the small

\*Received by the editors January 10, 2022; accepted for publication (in revised form) November 15, 2022; published electronically April 28, 2023.

<https://doi.org/10.1137/22M1470074>

<sup>†</sup>Department of Mathematics, College of Engineering and Physical Science, Aston University, Birmingham, UK (nhane22@aston.ac.uk).

<sup>‡</sup>Department of Mathematics and Statistics, University of Limerick, Limerick, Ireland (doireann.okiely@ul.ie, <http://www.doireannokiely.com>).

aspect ratio  $\epsilon$  of radius to length of the fiber, either by assuming the fiber radius is slowly varying [18] or via asymptotic expansion in the small aspect ratio [27]. Variations on this approach have been used to investigate the stability of the steady state (i.e., draw resonance) [25, 15], to quantify the role of different effects such as gravity, inertia, surface tension, and magnetism [18, 30], and to investigate the evolution of microstructure and cross-sectional profile [8, 11, 12, 20, 21]. Coupling between heat and fluid flow is also a major point of interest in glass drawing processes, where elongation is typically localized in the neighborhood where temperature is highest and viscosity is lowest [29, 28]. Stability is also a topic of major interest [24, 25, 15, 26].

Most of the modeling work carried out to date has involved either calculating the leading-order behavior in the limit as the aspect ratio  $\epsilon \rightarrow 0$  [18, 6] or numerical solution of the two- or three-dimensional governing equations, e.g., [7]. Schultz and Davis [27] extended the asymptotic expansion in powers of  $\epsilon^2$  and presented a calculation for correction terms at this order, while Page et al. [23] investigated adjustments to the flow profile due to radially dependent viscosity. However, recent analysis of glass sheet redraw demonstrated that boundary layers at the sheet ends play a significant role in determining corrections to the leading order and can even give rise to corrections which are actually  $O(\epsilon)$  [21]. In this paper we use a combination of finite element and asymptotic analysis to analyze the correction terms in the case of drawing of a circular fiber. We show that the first nonzero correction terms are  $O(\epsilon)$  for applied inlet and outlet velocities, an order of magnitude larger than those calculated previously, and are  $O(\epsilon^2)$  for applied inlet and outlet stresses.

The paper is organized as follows. In section 2 we outline the governing equations for an axisymmetric viscous cylinder with fluid flow driven by either applied velocities or applied stresses at inlet and outlet positions. We nondimensionalize and introduce an aspect ratio  $\epsilon$ . In section 3 we present numerical solutions and highlight the rapid adjustment of the flow profile between its one-dimensional bulk behavior and the applied conditions near the inlet and outlet in the case of applied velocities. In section 4 we present an asymptotic analysis of the long, slender limit  $\epsilon \rightarrow 0$ . We reproduce the classic Trouton model at leading order. We introduce linear differential equations for  $O(\epsilon)$  corrections whose solution may be nonzero if nonhomogeneous boundary conditions are applied. Assessment of the leading-order solution reveals boundary layers at the fiber ends, which are analyzed in section 5. This boundary-layer analysis both resolves the rapid adjustment of the leading-order solution near the inlet and outlet and yields correct boundary conditions for the  $O(\epsilon)$  corrections. Crucially, these boundary conditions are nonhomogeneous, and  $O(\epsilon)$  corrections to the leading-order Trouton model are predicted. These corrections are presented in section 6 and are in excellent agreement with numerical solutions. We conclude by discussing alternative boundary conditions and temperature effects in sections 7 and 8, followed by a discussion in section 9.

## 2. Governing equations.

**2.1. Two-dimensional axisymmetric model.** We consider steady-state, axisymmetric drawing of a thread of Newtonian fluid and assume that inertia and gravity are negligible. We neglect temperature effects and assume that the fiber has a uniform viscosity  $\mu^*$ , although the analysis presented here can be extended to an axially varying viscosity as outlined in Appendix A. We use cylindrical polar coordinates centered in the middle of the fiber at the beginning of the draw zone, with  $z^*$  pointing along the fiber axis in the direction of fiber drawing and  $r^*$  pointing in the radial

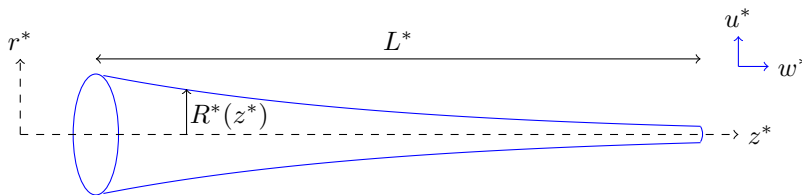


FIG. 1. Schematic of fiber drawing.

direction as shown in Figure 1. We denote the radial and axial velocities by  $u^*$  and  $w^*$ , respectively, and the pressure by  $p^*$ . Conservation of mass and momentum in the fiber are described by

$$(2.1) \quad \frac{1}{r^*} \frac{\partial}{\partial r^*} (r^* u^*) + \frac{\partial w^*}{\partial z^*} = 0,$$

$$(2.2) \quad -\frac{\partial p^*}{\partial r^*} + \mu^* \frac{\partial}{\partial r^*} \left[ \frac{1}{r^*} \frac{\partial}{\partial r^*} (r^* u^*) \right] + \mu^* \frac{\partial^2 u^*}{\partial z^{*2}} = 0,$$

$$(2.3) \quad -\frac{\partial p^*}{\partial z^*} + \mu^* \frac{1}{r^*} \frac{\partial}{\partial r^*} \left( r^* \frac{\partial w^*}{\partial r^*} \right) + \mu^* \frac{\partial^2 w^*}{\partial z^{*2}} = 0,$$

where the radial momentum equation (2.2) includes a contribution from the axisymmetric hoop stress  $-p^* + 2\mu^* u^*/r^*$ . The fiber radius is not known a priori and must be determined as part of the problem solution; we denote it by  $r^* = R^*(z^*)$ . We impose no-flux and no-stress conditions (neglecting surface tension) at this free boundary via

$$(2.4) \quad u^* = \frac{dR^*}{dz^*} w^*,$$

$$(2.5) \quad \left( -p^* + 2\mu^* \frac{\partial u^*}{\partial r^*} \right) = \frac{dR^*}{dz^*} \left[ \mu^* \left( \frac{\partial w^*}{\partial r^*} + \frac{\partial u^*}{\partial z^*} \right) \right],$$

$$(2.6) \quad \mu^* \left( \frac{\partial w^*}{\partial r^*} + \frac{\partial u^*}{\partial z^*} \right) = \frac{dR^*}{dz^*} \left( -p^* + 2\mu^* \frac{\partial w^*}{\partial z^*} \right)$$

at  $r^* = R^*(z^*)$ .

**2.2. Inlet and outlet conditions.** The fiber enters the drawing zone at a known radius

$$(2.7) \quad R^*(0) = R_{\text{in}}^*.$$

The acceleration required for thinning of the viscous thread is driven by a mismatch between velocities imposed at the inlet and outlet to the stretching zone: increasing the axial velocity by a factor  $D$  leads to a reduction in radius by a factor  $1/\sqrt{D}$ . The mechanism by which material enters the stretching zone varies between industries: for fiber-optic cables, a solid cylinder known as a preform is fed into a furnace, where it is heated and stretched, while for polymer drawing, liquid polymer is usually extruded through a die into the stretching zone. At the outlet, the material exits the stretching zone at an outlet velocity that is larger than the inlet velocity, which may be controlled directly or via an applied tension. We consider three different scenarios:

1. Uniform velocity: The fiber enters and exits the stretching zone via rigid body translation, and a pressure condition is applied to close the problem, so

$$(2.8a) \quad w^* = w_{\text{in}}^*, \quad u^* = 0 \quad \text{at} \quad z^* = 0,$$

$$(2.8b) \quad p^* = 0 \quad \text{at} \quad z^* = 0,$$

$$(2.8c) \quad w^* = w_{\text{out}}^*, \quad u^* = 0 \quad \text{at} \quad z^* = L^*,$$

where  $w_{\text{in}}^*$  and  $w_{\text{out}}^*$  are the inlet and outlet velocities and  $L^*$  is the length of the stretching zone.

2. Applied tension: A uniform axial stress and zero shear stress are applied at the inlet and outlet, and a uniform inlet axial velocity is applied to close the problem, so

$$(2.9a) \quad \left. \begin{aligned} \sigma_{zz}^* &= -p^* + 2\mu^* \frac{\partial w^*}{\partial z^*} = \sigma_{\text{in}}^*, \\ \sigma_{rz}^* &= \mu^* \left( \frac{\partial u^*}{\partial z^*} + \frac{\partial w^*}{\partial r^*} \right) = 0, \\ w^* &= w_{\text{in}}^* \end{aligned} \right\} \quad \text{at} \quad z^* = 0,$$

$$(2.9b) \quad \left. \begin{aligned} \sigma_{zz}^* &= -p^* + 2\mu^* \frac{\partial w^*}{\partial z^*} = \sigma_{\text{out}}^*, \\ \sigma_{rz}^* &= \mu^* \left( \frac{\partial u^*}{\partial z^*} + \frac{\partial w^*}{\partial r^*} \right) = 0 \end{aligned} \right\} \quad \text{at} \quad z^* = L^*.$$

3. Pipe flow: For die extrusion the fiber enters through a tube and may have a radially varying axial velocity, e.g., Poiseuille; in this case we might impose

$$(2.10) \quad w^* = 2w_{\text{in}}^* \left( 1 - \frac{r^2}{(R_{\text{in}}^*)^2} \right), \quad u^* = 0 \quad \text{at} \quad z^* = 0,$$

together with an inlet pressure and either uniform velocity or applied stress outlet conditions.

Combinations of these conditions could also be applied, but we focus here on cases 1 and 2, and radially varying inlet profiles are discussed briefly in section 7.

**2.3. Nondimensionalization.** We nondimensionalize by defining  $\epsilon = R_{\text{in}}^*/L^*$  and introducing

$$(2.11a) \quad (z, r) = \left( \frac{z^*}{L^*}, \frac{r^*}{\epsilon L^*} \right), \quad (w, u) = \left( \frac{w^*}{w_{\text{in}}^*}, \frac{u^*}{\epsilon w_{\text{in}}^*} \right), \quad p = \frac{p^*}{\mu^* w_{\text{in}}^*/L^*}, \quad R = \frac{R^*}{R_{\text{in}}^*},$$

$$(2.11b) \quad p = \frac{p^*}{\mu^* w_{\text{in}}^*/L^*}, \quad \sigma_{ii} = \frac{\sigma_{ii}^*}{\mu^* w_{\text{in}}^*/L^*}, \quad \sigma_{rz} = \frac{\sigma_{rz}^*}{\epsilon^{-1} \mu^* w_{\text{in}}^*/L^*}.$$

Substituting these dimensionless variables into the governing equations (2.1)–(2.8) yields mass and momentum equations

$$(2.12) \quad \frac{1}{r} \frac{\partial}{\partial r} (ru) + \frac{\partial w}{\partial z} = 0,$$

$$(2.13) \quad -\frac{\partial p}{\partial r} + \frac{\partial}{\partial r} \left[ \frac{1}{r} \frac{\partial}{\partial r} (ru) \right] + \epsilon^2 \frac{\partial^2 u}{\partial z^2} = 0,$$

$$(2.14) \quad -\frac{\partial p}{\partial z} + \epsilon^{-2} \frac{1}{r} \frac{\partial}{\partial r} \left( r \frac{\partial w}{\partial r} \right) + \frac{\partial^2 w}{\partial z^2} = 0,$$

together with free-boundary conditions

$$(2.15) \quad u = \frac{dR}{dz} w,$$

$$(2.16) \quad -p + 2 \frac{\partial u}{\partial r} = \frac{dR}{dz} \left( \frac{\partial w}{\partial r} + \epsilon^2 \frac{\partial u}{\partial z} \right),$$

$$(2.17) \quad \epsilon^{-2} \frac{\partial w}{\partial r} + \frac{\partial u}{\partial z} = \frac{dR}{dz} \left( -p + 2 \frac{\partial w}{\partial z} \right),$$

at  $r = R(z)$ . We also require all quantities to be regular at  $r = 0$ , so the radial velocity and (axisymmetric) shear stress are both zero there.

For applied inlet and outlet velocities (case 1), we obtain

$$(2.18) \quad w = R = 1, \quad u = p = 0 \quad \text{at } z = 0,$$

$$(2.19) \quad w = D, \quad u = 0 \quad \text{at } z = 1,$$

where  $D = w_{\text{out}}^*/w_{\text{in}}^*$  is referred to as the draw ratio. For applied inlet and outlet stresses (case 2), we obtain

$$(2.20a) \quad w = R = 1 \quad \text{at } z = 0,$$

$$(2.20b) \quad \sigma_{zz} = -p + 2 \frac{\partial w}{\partial z} = \sigma_{\text{in}}, \quad \sigma_{rz} = \epsilon^2 \frac{\partial u}{\partial z} + \frac{\partial w}{\partial r} = 0 \quad \text{at } z = 0,$$

$$(2.20c) \quad \sigma_{zz} = -p + 2 \frac{\partial w}{\partial z} = \sigma_{\text{out}}, \quad \sigma_{rz} = \epsilon^2 \frac{\partial u}{\partial z} + \frac{\partial w}{\partial r} = 0 \quad \text{at } z = 1,$$

where  $\sigma_{\text{in}} = \sigma_{\text{in}}^* L^* / \mu^* w_{\text{in}}^*$  and  $\sigma_{\text{out}} = \sigma_{\text{out}}^* L^* / \mu^* w_{\text{in}}^*$  are dimensionless axial stresses, which must be chosen to give a desired increase in axial velocity.

**2.4. Averaged quantities.** In section 4 we will also utilize cross-sectionally averaged versions of the mass and axial momentum equations. These are obtained by integrating (2.12) and (2.14) across the fiber radius and applying the no-flux and no-stress boundary conditions (2.15) and (2.17). We do the second calculation by first rewriting (2.14) in terms of  $-p + 2\partial w/\partial z$  and  $\partial u/\partial z + \partial w/\partial r$  using (2.12). We then find

$$(2.21) \quad \frac{d}{dz} \int_0^{R(z)} r w \, dr = 0,$$

$$(2.22) \quad \frac{d}{dz} \int_0^{R(z)} r \left[ -p + 2 \frac{\partial w}{\partial z} \right] dr = 0.$$

**3. Numerical solution.** We solve the full two-dimensional problem (2.12)–(2.17) numerically using the finite element software FEniCS [17], mapping the problem onto a fixed domain via a change of variables [16, 4, 21],

$$(3.1) \quad \eta = \frac{r}{R(z)}, \quad \zeta = z.$$

The domain  $[\eta, \zeta] \in [0, 1] \times [0, 1]$  is triangulated using a  $100 \times 96$  mesh for  $\zeta \in [0.2, 0.98]$  and 16 times higher resolution in  $\zeta$  for  $\zeta \in [0, 0.2]$  and  $\zeta \in [0.98, 1]$ . The increased

resolution near the inlet and outlet was required to accurately resolve rapid changes in the solution in these zones. The numerical scheme used quadratic test functions for velocity components and fiber radius and a linear test function for pressure. Further details of the solution procedure are given in Appendix B.

Plots of the numerical solution are shown in Figure 2 for case 1, i.e., applied velocities. A draw ratio  $D = 30$  and an aspect ratio  $\epsilon = 0.1$  were used in this case, but the solutions for other values of  $D$  and of  $\epsilon \ll 1$  are similar. Solutions for cases 1 and 2 are shown together in Figure 3, with stresses  $\sigma_{\text{in}}^* = 3 \log(30)$  and  $\sigma_{\text{out}}^* = 3 \times 30 \log(30)$  which will be justified in section 4.1. The solutions are very similar apart from in small regions near the boundaries. In Figure 2, the velocity in the  $z$ -direction is approximately uniform across the fiber radius and increases from  $w(r, 0) = 1$  at the inlet to  $w(r, 1) = 30$  at the outlet, as required by the boundary conditions (see Figure 2(a)). The fiber radius decreases (highlighted in Figure 2(b)) from  $R(0) = 1$  to  $R(1) = 1/\sqrt{30} \approx 0.18$  as expected. The transverse velocity is directed radially inward (see Figure 2(c)), which is consistent with a decreasing fiber radius, and its magnitude appears to increase linearly with distance from the central axis (see inset). The radial velocity and pressure both exhibit rapid changes near the inlet and outlet for applied velocities (see Figure 2(c) and (d) or Figure 3(c) and (d)), but not for applied tensions; we will analyze this further via asymptotic analysis below. We also note that applying a velocity boundary condition at the outlet leads to a pressure singularity at the corner  $z = 1, r = R(1)$ . Such a singularity is common when there is a sudden change in boundary conditions (see, e.g., [9]), and we note that it disappears when stress conditions are applied instead.

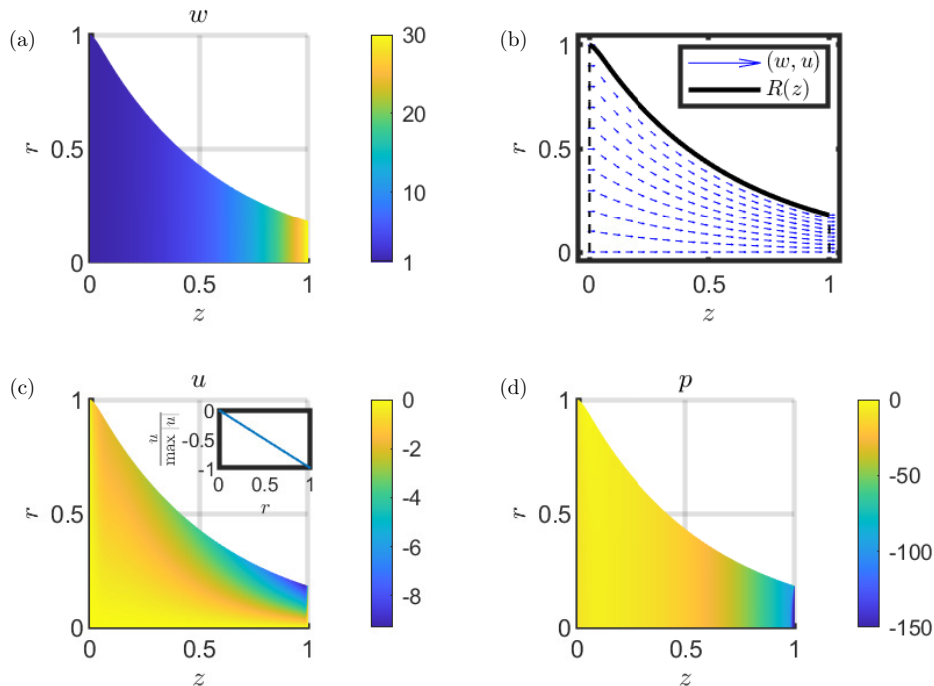


FIG. 2. Numerical solution to fiber-drawing equations (2.12)–(2.19), with velocity boundary conditions (case 1), for draw ratio  $D = 30$  and aspect ratio  $\epsilon = 0.1$ : (a) axial velocity, (b) flow profile, with fiber radius  $R(z)$  highlighted in black, (c) radial velocity, with  $u$  evaluated at  $z = 0.5$  in the inset, and (d) pressure.

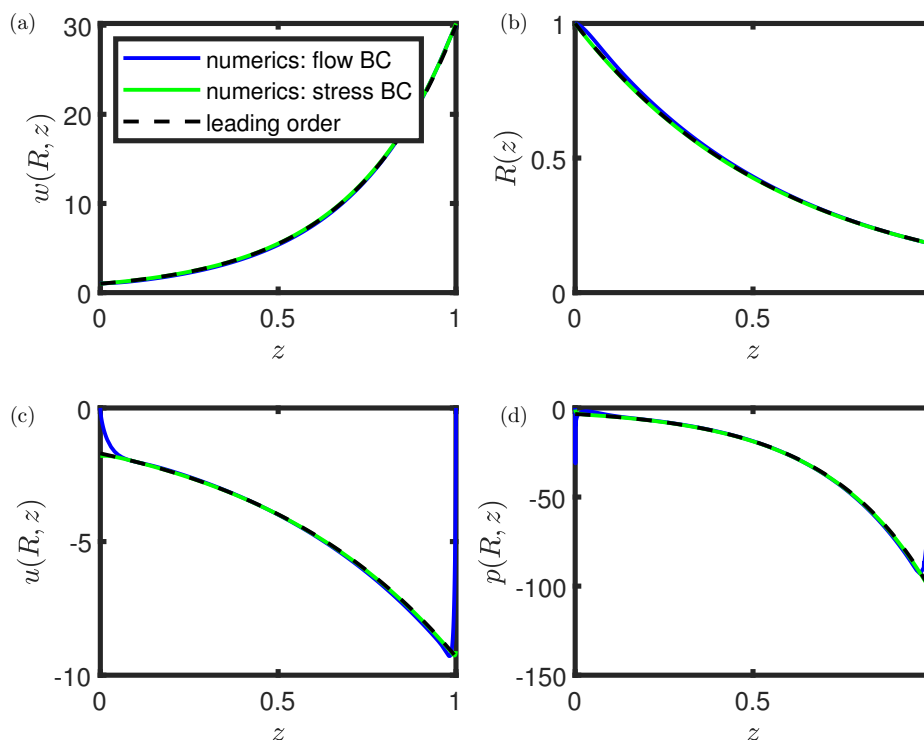


FIG. 3. Leading-order solutions for velocity, pressure, and fiber radius, compared with numerical solutions evaluated on the fiber surface for  $\epsilon = 0.1$ ,  $D = 30$ .

**4. Asymptotic analysis.** We exploit the fact that the aspect ratio  $\epsilon$  is small by expanding the pressure, velocities, and fiber radius in powers of  $\epsilon$  and taking the limit  $\epsilon \rightarrow 0$ . The radial velocity, for example, is rewritten as

$$u = u_0 + \epsilon u_1 + \epsilon^2 u_2 + \epsilon^3 u_3 + \dots$$

The derivation outlined below for the leading-order quantities is standard and can be found throughout the literature, for example, in [27, 6, 14, 8]. However, here an analogous derivation for the  $O(\epsilon)$  terms is also carried out. The procedure is the same at both orders so the two are carried out together.

**4.1. Bulk equations.** Evaluating the axial momentum equation (2.14) and corresponding boundary condition (2.17) at  $O(1)$  immediately yields the result that the axial velocity does not vary with radius up to  $O(\epsilon^2)$ , i.e.,

$$(4.1) \quad w_0 = W_0(z), \quad w_1 = W_1(z).$$

It then follows from the continuity equation (2.12) that the radial velocity is linear in  $r$  at these orders, i.e.,

$$(4.2) \quad u_0 = -\frac{r}{2} W_0'(z), \quad u_1 = -\frac{r}{2} W_1'(z),$$

where we have used the requirement of zero radial velocity at the center of the fiber to determine the constants of integration. These profiles are consistent with the

numerical solutions presented in section 3. Following a similar procedure with the radial momentum equation (2.13) and corresponding boundary condition (2.16) yields

$$(4.3) \quad p_0 = -W'_0(z), \quad p_1 = -W'_1(z),$$

so the pressure is approximately uniform across the sheet thickness and is related directly to the velocity gradient. We can now close the problem for the functions  $W_0$  and  $R_0$  by evaluating the averaged equations (2.21) and (2.22) at leading order to find

$$(4.4) \quad \frac{d}{dz} (R_0^2 W_0) = 0, \quad \frac{d}{dz} (3R_0^2 W'_0) = 0.$$

Integrating the leading-order equations (4.4) and applying the inlet and outlet conditions (2.18) and (2.19) yields

$$(4.5) \quad W_0(z) = D^z, \quad R_0(z) = D^{-z/2}.$$

The same solution is obtained for the inlet and outlet conditions (2.20) if the stresses are chosen to be  $\sigma_{\text{in}} = 3 \ln(D)$  and  $\sigma_{\text{out}} = 3D \ln(D)$ .

The full leading-order solution is therefore

$$(4.6) \quad w_0 = D^z,$$

$$(4.7) \quad R_0 = D^{-z/2},$$

$$(4.8) \quad u_0 = -\frac{r}{2} \ln(D) D^z,$$

$$(4.9) \quad p_0 = -\ln(D) D^z.$$

We compare the leading-order solution (4.6)–(4.9) to the numerical solution from section 3 in Figure 3 for an aspect ratio  $\epsilon = 0.1$  and draw ratio  $D = 30$ . The fiber radius and axial velocity are in excellent agreement with the numerical solutions throughout the domain. The radial velocity and pressure are also in good agreement, except for small regions near the inlet and outlet in the case of an applied inlet and outlet velocity field, where the numerical solution adjusts rapidly to satisfy the boundary conditions. We note here that the leading-order radial velocity  $u_0 = -(r/2)w'_0(z) = -(r/2) \ln(D) D^z$  and pressure  $p_0 = -w'_0(z) = -\ln(D) D^z$  follow directly from the axial velocity profile and cannot satisfy general inlet and outlet conditions, including the conditions (2.18)–(2.19) for an applied velocity field. This suggests that there are two-dimensional boundary layers near the inlet and outlet where the fluid velocity adjusts from the imposed boundary conditions to the one-dimensional bulk solution. We analyze these boundary layers in sections 5.1–5.3.

We can repeat the derivation procedure outlined above to find governing equations for the  $O(\epsilon)$  variables by evaluating the averaged equations (2.21), (2.22) to give

$$(4.10) \quad \frac{d}{dz} (R_0^2 W_1 + 2R_0 R_1 W_0) = 0, \quad \frac{d}{dz} [3(R_0^2 W'_1 + 2R_0 R_1 W'_0)] = 0,$$

where the prime ( $'$ ) denotes differentiation with respect to  $z$ . If we solved these equations subject to  $R_1 = W_1 = 0$  at the inlet and outlet, we would find that the  $O(\epsilon)$  corrections are identically zero. However, the occurrence of boundary layers near  $z = 0$  and  $z = 1$  suggests that there may be nonzero boundary conditions and hence nonzero corrections; we investigate this further in section 5.



**4.2. Error quantification.** We analyze the performance of the leading-order solution (4.6)–(4.9) by calculating the error compared with the numerical solution from section 3; see Figure 4. The deviation from leading-order is larger for case 1 than case 2, and neither is captured accurately by the Schultz and Davis [27] prediction

$$(4.11) \quad R_{SD}(z) = D^{-z/2} + \epsilon^2 \frac{(\ln D)^2}{16} \left[ z \left( 1 - \frac{1}{D} \right) - \left( 1 - \frac{1}{D^z} \right) \right] D^{-z/2} + O(\epsilon^4),$$

$$(4.12) \quad w_{SD}(r, z) = D^z + \epsilon^2 \frac{(\ln D)^2}{8} \left\{ \left[ -4r^2 + 1 - z \left( 1 - \frac{1}{D} \right) \right] D^z + 1 \right\} + O(\epsilon^4).$$

We investigate further by examining the size of the deviation as a function of the small aspect ratio  $\epsilon$ ; for simplicity we evaluate on the free boundary at particular values of  $z$  that are not near sign changes in error. We carry out the calculation for three different mesh densities to ensure numerical convergence. The error increases linearly with  $\epsilon$  in the case of applied velocity fields and quadratically with  $\epsilon$  in the case of applied stress fields (see Figure 5). This suggests that the first corrections in the asymptotic expansion should be of  $O(\epsilon)$  for at least some boundary conditions, which is in contrast to [27], where corrections are assumed to be  $O(\epsilon^2)$ . Since applied velocity fields correspond to a worst-case scenario with  $O(\epsilon)$  deviations from leading order, we concentrate on modeling and explaining that scenario in the sections below.

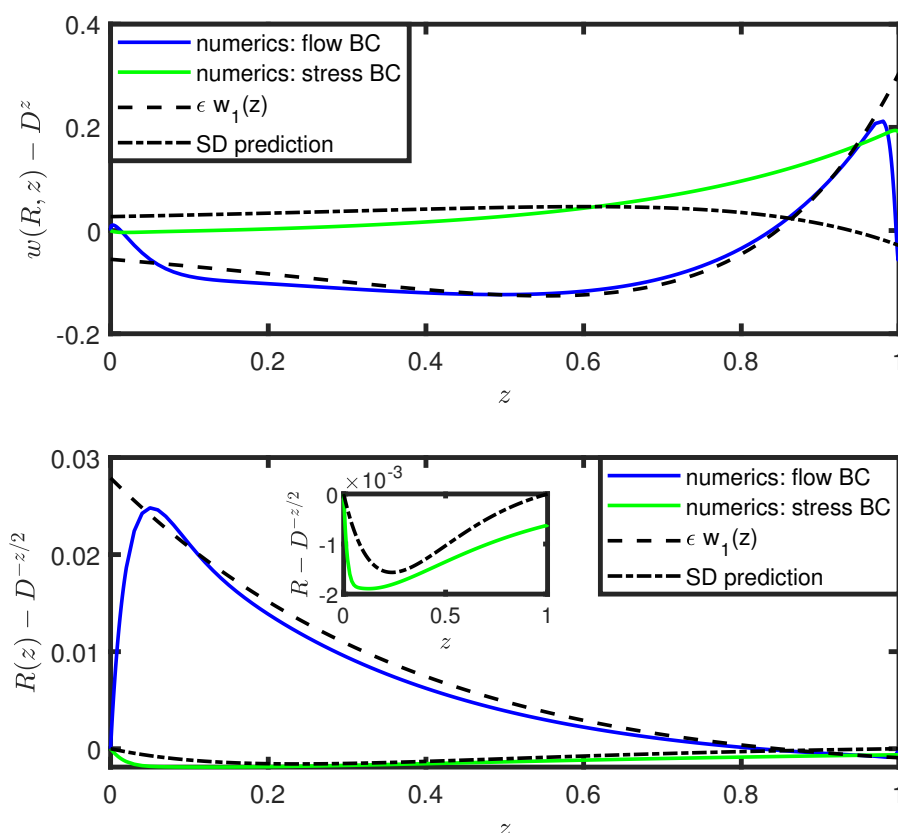


FIG. 4. Corrections to the leading-order predictions  $w \approx D^z$  and  $R \approx D^{-z/2}$  for  $\epsilon = 0.05$ : the numerical solution from section 3 is compared to the asymptotic solutions  $\epsilon w_1$  and  $\epsilon R_1$  given by (6.5) and (6.6), respectively. The  $O(\epsilon^2)$  prediction from [27] is included for reference.

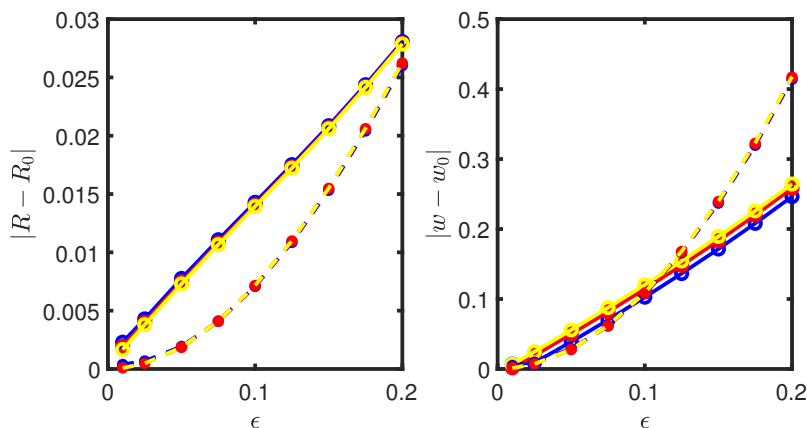


FIG 5. Errors in the leading-order Trouton model (4.6)–(4.9) compared to the numerical solution to (2.12)–(2.17). The axial velocity is evaluated on the free boundary at  $z = 0.5$ , while the fiber radius is evaluated at  $z = 0.2$ . The three colors correspond to three mesh densities: blue is the mesh described in section 3, red has 1/2 as many mesh points, and yellow has 1/4 as many mesh points. The solid curves are for case 1, i.e., inlet and outlet velocity conditions, while the dashed curves are for case 2, i.e., inlet and outlet stress conditions.

## 5. Boundary-layer analysis.

**5.1. Inlet boundary layer.** Since the one-dimensional leading-order solution (4.8) cannot satisfy an inlet boundary condition  $u_0(0) = 0$ , we consider a boundary layer of size  $\epsilon$  where two-dimensional effects will appear at leading order. We rescale into this boundary layer by defining

$$(5.1) \quad z = \epsilon \bar{z}, \quad r = \bar{r}.$$

We anticipate matching the boundary-layer solution as  $\bar{z} \rightarrow \infty$  to the bulk solution (4.6)–(4.9) as  $z \rightarrow 0$ , so we propose boundary-layer solutions of the form

$$(5.2) \quad w(r, z) = 1 + \epsilon \ln(D) (\bar{z} + \bar{w}(\bar{r}, \bar{z})) + \dots,$$

$$(5.3) \quad R(z) = 1 + \epsilon \ln(D) \left( -\frac{\bar{z}}{2} + \bar{R}(\bar{z}) \right) + \dots,$$

$$(5.4) \quad u(r, z) = \ln(D) \left( -\frac{\bar{r}}{2} + \bar{u}(\bar{r}, \bar{z}) \right) + \dots,$$

$$(5.5) \quad p(r, z) = \ln(D) (-1 + \bar{p}(\bar{r}, \bar{z})) + \dots.$$

We now substitute the change of variables and expansion into the full dimensionless problem (2.12)–(2.17). This results in a canonical leading-order boundary-layer problem

$$(5.6) \quad \frac{1}{\bar{r}} \frac{\partial}{\partial \bar{r}} (\bar{r} \bar{u}) + \frac{\partial \bar{w}}{\partial \bar{z}} = 0,$$

$$(5.7) \quad -\frac{\partial \bar{p}}{\partial \bar{r}} + \frac{\partial}{\partial \bar{r}} \left[ \frac{1}{\bar{r}} \frac{\partial}{\partial \bar{r}} (\bar{r} \bar{u}) \right] + \frac{\partial^2 \bar{u}}{\partial \bar{z}^2} = 0,$$

$$(5.8) \quad -\frac{\partial \bar{p}}{\partial \bar{z}} + \frac{1}{\bar{r}} \frac{\partial}{\partial \bar{r}} \left( \bar{r} \frac{\partial \bar{w}}{\partial \bar{r}} \right) + \frac{\partial^2 \bar{w}}{\partial \bar{z}^2} = 0.$$

Since the free boundary is located at  $\bar{r} = r = R = 1 + O(\epsilon)$ , the conditions there can be linearized onto  $\bar{r} = 1$ , and so the no-stress conditions there yield

$$(5.9) \quad -\bar{p} + 2 \frac{\partial \bar{u}}{\partial \bar{r}} = 0,$$

$$(5.10) \quad \frac{\partial \bar{w}}{\partial \bar{r}} + \frac{\partial \bar{u}}{\partial \bar{z}} = 0.$$

The corresponding inlet and far-field conditions are given by

$$(5.11) \quad \bar{w} = 0, \quad \bar{u} = \frac{\bar{r}}{2}, \quad \bar{p} = 1 \quad \text{at} \quad \bar{z} = 0,$$

$$(5.12) \quad \bar{u}, \bar{p} \rightarrow 0 \quad \text{as} \quad \bar{z} \rightarrow \infty.$$

The correction to the fiber radius inside the boundary layer is then given by

$$(5.13) \quad \frac{d\bar{R}}{d\bar{z}} = \bar{u}(1, \bar{z}), \quad \bar{R}(\bar{z} = 0) = 0.$$

This boundary-layer problem must be solved numerically but is independent of the draw ratio  $D$ , so it only needs to be solved once and the solution can then be rescaled for any draw ratio and aspect ratio. We carry out the numerical solution in section 5.3, but we first derive the governing equations in the boundary layer near the outlet.

**5.2. Outlet boundary layer.** In the boundary layer near the outlet we anticipate that the fiber radius will be approximately  $1/\sqrt{D}$ , so we rescale into the boundary layer and simultaneously scale the governing equations onto a domain of radius 1 by defining

$$(5.14) \quad z = 1 - \epsilon D^{-1/2} \bar{z}, \quad r = D^{-1/2} \bar{r}.$$

We reuse the bar notation from section 5.1 in anticipation that the inlet and outlet zones will correspond to scaled versions of the same system. Inspired by the canonical inlet problem derived in section 5.1, we aim to eliminate the draw ratio from the governing equations. To this end, we carry out a boundary-layer rescaling for the velocity and pressure

$$(5.15) \quad w(r, z) = D \left[ 1 - \epsilon D^{-1/2} \ln(D) (\bar{z} + \bar{w}(\bar{r}, \bar{z})) + \cdots \right],$$

$$(5.16) \quad R(z) = D^{-1/2} \left[ 1 - \epsilon D^{-1/2} \ln(D) \left( -\frac{\bar{z}}{2} + \bar{R}(\bar{z}) + c_{out} \right) + \cdots \right],$$

$$(5.17) \quad u(r, z) = D^{1/2} \ln(D) \left( -\frac{\bar{r}}{2} + \bar{u}(\bar{r}, \bar{z}) \right) + \cdots,$$

$$(5.18) \quad p(r, z) = D \ln(D) (-1 + \bar{p}(\bar{r}, \bar{z})) + \cdots,$$

where repeated use of barred variables and the inclusion of the constant  $c_{out}$  in the expansion for  $R$  will both be explained below. Substituting the expansion (5.15)–(5.18) into the governing equations (2.12)–(2.17) yields the same governing equations (5.6)–(5.13) for the outlet boundary layer as for the inlet boundary layer. The fiber radius is not imposed at the outlet so we do not immediately have a boundary condition at  $\bar{z} = 0$ . Ultimately, the fiber radius in the boundary layer will be required to match the fiber radius in the bulk as  $z \rightarrow 1$ , which we will calculate in section 6. For now, we close the problem under consideration here by introducing an offset  $c_{out}$  such

that  $\bar{R}(0) = 0$  and the outlet problem matches the inlet one exactly. We anticipate that  $c_{out} = 0$  since the final radius should be exactly  $1/\sqrt{D}$  by conservation of mass, but we confirm this in section 6.

The inflow and outflow boundary layers are now described in terms of a single canonical boundary-layer problem (5.6)–(5.13).

**5.3. Numerical solution.** The canonical boundary-layer problem (5.6)–(5.13) was solved numerically using FEniCS [17]. We note that the problem is defined on a fixed but semi-infinite domain  $\bar{r} \in [0, 1]$ ,  $\bar{z} \in [0, \infty)$ , which was truncated for the numerical solution at  $\bar{z} = 10$ . The numerical solutions are shown in Figure 6, truncated at  $\bar{z} = 3$  for visibility. We observe that both velocity components vary in both directions inside the boundary layer. The correction to the fiber radius exhibits a slight bump, associated with the slight decrease in axial velocity as the radial velocity adjusts to its bulk profile. We note that the pressure exhibits a singularity at  $\bar{z} = 0$ ,  $\bar{r} = 1$ : this corresponds to the singularities at  $z = 0$  and  $z = 1$  in the solution of the full problem (Figure 3).

**5.4. Far-field behavior.** We will determine the corrections to the bulk solution by matching with the boundary-layer solutions at either end of the fiber. Numerical evaluation of the values of  $\bar{w}$  and  $\bar{R}$  in the far field yields

$$(5.19) \quad \bar{w}(\bar{z} \rightarrow \infty) = c_w = -0.164,$$

$$(5.20) \quad \bar{R}(\bar{z} \rightarrow \infty) = c_R = 0.082.$$

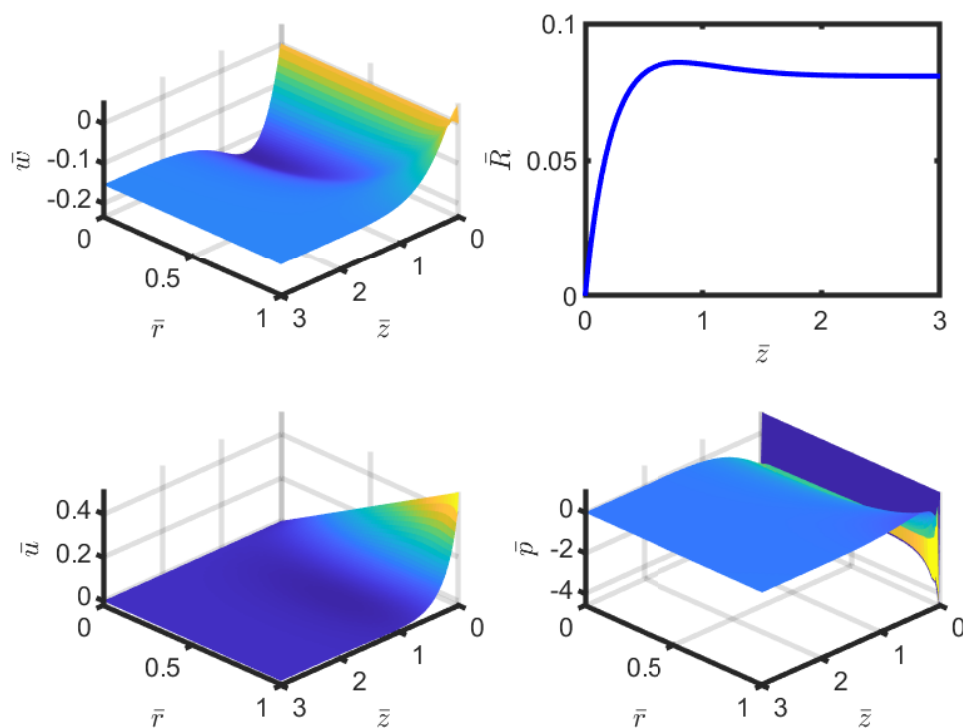


FIG. 6. Numerical solutions for  $\bar{w}$ ,  $\bar{u}$ ,  $\bar{R}$ , and  $\bar{p}$  from the boundary-layer problem (5.6)–(5.13).

We note that the far-field value of  $\bar{R}$  appears to be  $-1/2$  times the far-field value of  $\bar{w}$ . In fact, this is an exact consequence of conservation of mass, which we can show as follows. Integrating the no-flux condition (5.13) along the free surface yields

$$(5.21) \quad \bar{R}(\bar{z} \rightarrow \infty) - \bar{R}(\bar{z} \rightarrow 0) = \int_0^\infty \bar{u}(1, \bar{z}) \, d\bar{z}.$$

Similarly, integrating the conservation of mass equation (5.6) over the entire boundary layer yields

$$(5.22) \quad \int_0^\infty \bar{u}(1, \bar{z}) \, d\bar{z} = -\frac{1}{2} [\bar{w}(\bar{z} \rightarrow \infty) - \bar{w}(\bar{z} = 0)]$$

since the  $\bar{w}$  is independent of  $\bar{z}$  at both ends. It then follows that  $c_R = -c_w/2$ .

**6. Corrections to the Trouton model.** From section 4, the  $O(\epsilon)$  corrections  $w_1$  and  $R_1$  to the leading-order solution are given by (4.10), which can be rewritten using the leading-order solutions (4.6)–(4.9) as

$$(6.1) \quad \frac{d}{dz} \left( D^{-z} w_1 + 2D^{z/2} R_1 \right) = 0,$$

$$(6.2) \quad \frac{d}{dz} \left[ 3 \left( D^{-z} \frac{dw_1}{dz} + 2 \ln(D) D^{z/2} R_1 \right) \right] = 0.$$

From section 5.3, the corresponding boundary conditions are

$$(6.3) \quad w_1 \rightarrow \ln(D) c_w, \quad R_1 \rightarrow -\frac{1}{2} \ln(D) c_w \quad \text{at } z \rightarrow 0,$$

$$(6.4) \quad w_1 \rightarrow -D^{\frac{1}{2}} \ln(D) c_w \quad \text{at } z \rightarrow 1.$$

The problem is satisfied by

$$(6.5) \quad w_1(z) = \ln(D) c_w \left[ 1 - \left( 1 + \frac{1}{\sqrt{D}} \right) z \right] D^z,$$

$$(6.6) \quad R_1(z) = -\frac{1}{2} \ln(D) c_w \left[ 1 - \left( 1 + \frac{1}{\sqrt{D}} \right) z \right] D^{-z/2}.$$

We compare these correction terms with the difference between the numerical and leading-order solutions for  $\epsilon = 0.1$  in Figure 4. We note that the numerical solution uses the same boundary conditions (2.18)–(2.19) as the asymptotic analysis. The correction  $\epsilon w_1$  is in excellent agreement with the estimate, except for in the boundary layers, where discrepancies should be expected. The literature prediction from [27] is shown for comparison and is both qualitatively and quantitatively different from the observed behavior. The scaled differences  $(w - w_0)/\epsilon$  collapse onto the single curve  $w_1$  for many values of  $\epsilon$  in Figure 7.

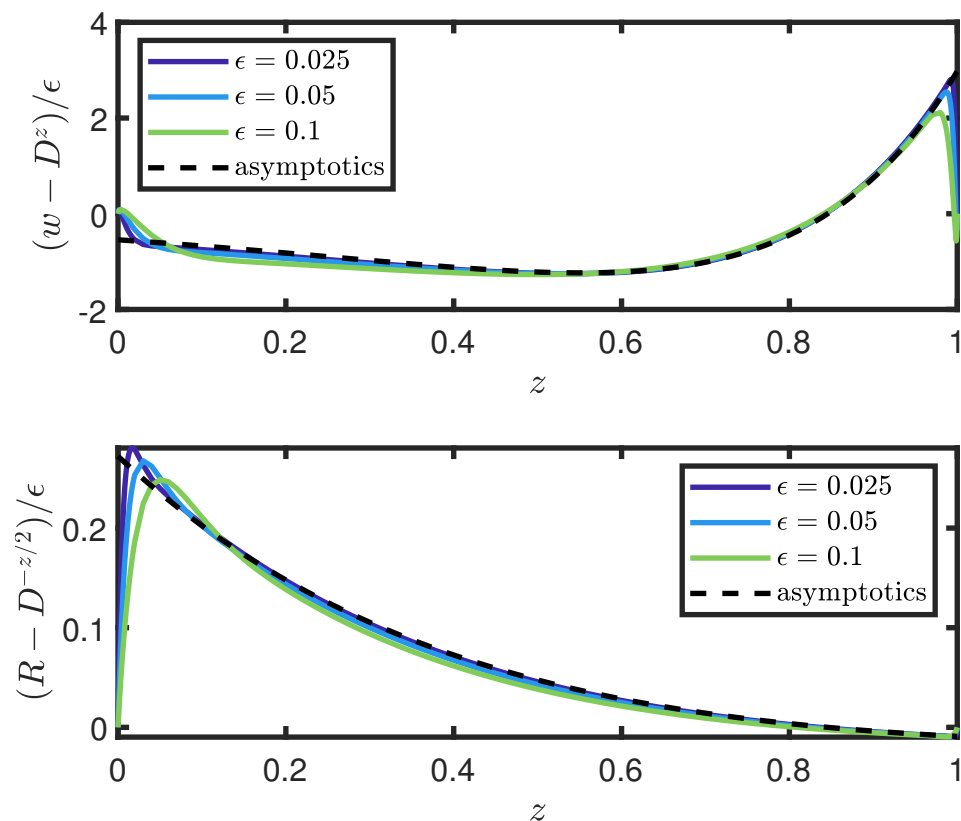


FIG. 7. Scaled difference between numerical and leading-order solutions, collapsed onto asymptotic solution (6.5)–(6.6).

The asymptotic approximation in the bulk of the sheet in the limit  $\epsilon \rightarrow 0$  can now be written

$$(6.7) \quad w(r, z) = D^z \left\{ 1 + \epsilon c_w \ln(D) \left[ 1 - \left( 1 + \frac{1}{\sqrt{D}} \right) z \right] \right\} + O(\epsilon^2),$$

$$(6.8) \quad R(z) = D^{-z/2} \left\{ 1 - \epsilon \frac{c_w}{2} \ln(D) \left[ 1 - \left( 1 + \frac{1}{\sqrt{D}} \right) z \right] \right\} + O(\epsilon^2),$$

$$(6.9) \quad u(r, z) = -\frac{r}{2} \ln(D) D^z \left\{ 1 + \epsilon c_w \left[ \ln(D) - \left( 1 + \frac{1}{\sqrt{D}} \right) (1 + \ln(D)z) \right] \right\} + O(\epsilon^2),$$

$$(6.10) \quad p(r, z) = -\ln(D) D^z \left\{ 1 + \epsilon c_w \left[ \ln(D) - \left( 1 + \frac{1}{\sqrt{D}} \right) (1 + \ln(D)z) \right] \right\} + O(\epsilon^2).$$

We note that the approximation (6.7)–(6.10) breaks down in boundary layers near the inlet and outlet and so should not be evaluated directly at  $z = 0$  and  $z = 1$ . To evaluate the final fiber radius we revisit the outlet boundary-layer expansion (5.16). Matching with the bulk solution as  $z \rightarrow 1$ , we find that the offset constant  $c_{out} = 0$  and so the final fiber radius is  $1/\sqrt{D}$ , as expected. We can now construct composite solutions

$$(6.11a) \quad w(r, z) \approx D^z + \epsilon c_w \ln D \left\{ \left[ 1 - \left( 1 + \frac{1}{\sqrt{D}} \right) z \right] D^z + \left[ \frac{\bar{w}(r, z/\epsilon)}{c_w} - 1 \right] - \sqrt{D} \left[ \frac{\bar{w}(r, \sqrt{D}(1-z)/\epsilon)}{c_w} - 1 \right] \right\},$$

$$(6.11b) \quad R(z) \approx D^{-z/2} - \epsilon \frac{c_w}{2} \ln D \left\{ \left[ 1 - \left( 1 + \frac{1}{\sqrt{D}} \right) z \right] D^{-z/2} - \left[ 1 + \frac{\bar{R}(z/\epsilon)}{c_w/2} \right] + \frac{1}{D} \left[ 1 + \frac{\bar{R}(\sqrt{D}(1-z)/\epsilon)}{c_w/2} \right] \right\},$$

which approximate the solution along the entire length of the fiber. This composite solution is shown in Figure 8 for an aspect ratio  $\epsilon = 0.1$  and draw ratio  $D = 30$ . The numerical, leading-order, and composite solutions for the axial velocity are indistinguishable on the scale of the plot, but there is a clear discrepancy between the numerical and leading-order solutions for the fiber radius, which is captured perfectly by the composite solution.

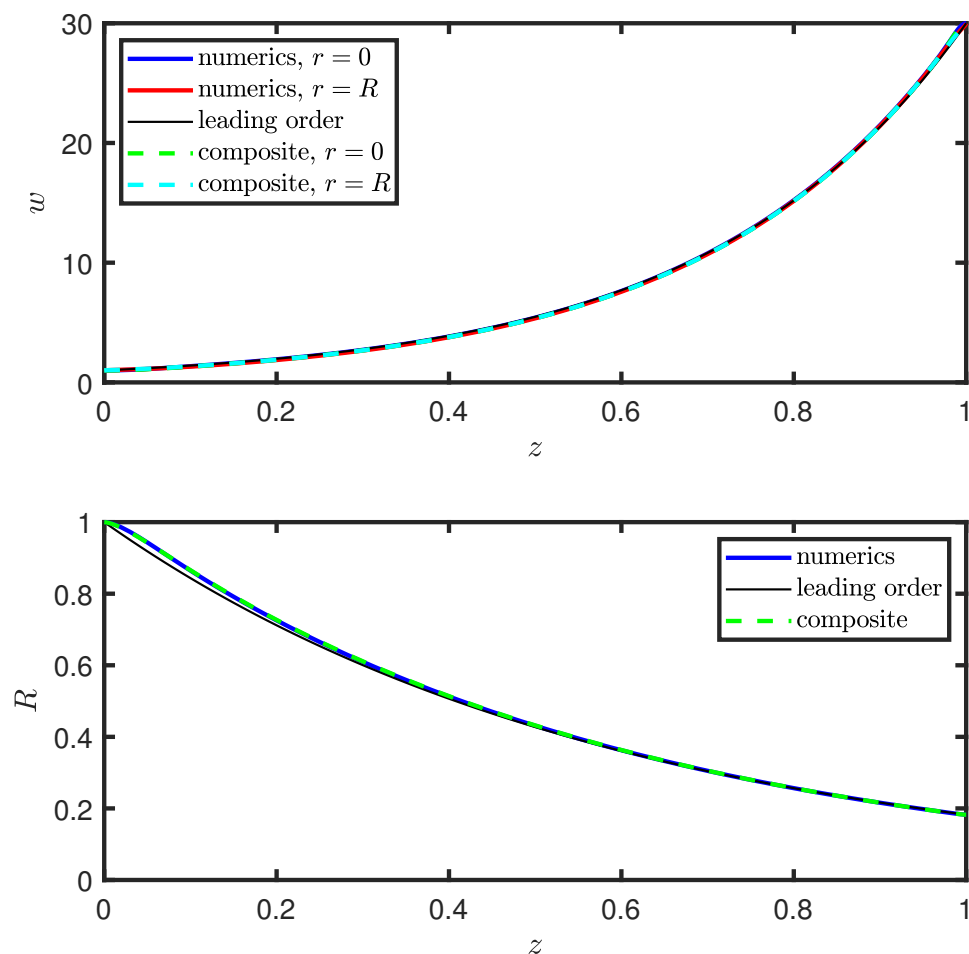


FIG. 8. Comparison between composite solution (6.11) and the numerical solution to (2.12)–(2.17) for aspect ratio  $\epsilon = 0.1$  and draw ratio  $D = 30$ .

## 7. Alternative boundary conditions.

**7.1. Stress condition.** When the leading-order velocity vector in the bulk of the sheet cannot satisfy the boundary conditions, boundary layers must be introduced at the sheet ends. In [27], the existence and importance of the boundary layers were obscured by the application of cross-sectionally averaged boundary conditions, which allowed for the derivation of a solution with no  $O(\epsilon)$  corrections, and instead  $O(\epsilon^2)$  terms were presented. Even though applying a uniform axial stress and zero shear stress eliminates the  $O(\epsilon)$  corrections, the corresponding  $O(\epsilon^2)$  corrections do not match those in [27]. This can be understood by noting that (4.12) is of the form  $w_2 = a(z)r^2 + b(z)$ ; this  $r$ -dependence still must be resolved across boundary layers if the inlet velocity is uniform, which in turn alters the boundary conditions required to determine  $a$  and  $b$ . The asymptotic analysis required to determine the corrections is likely to have industrial relevance and may therefore warrant further exploration in the future.

**7.2. Poiseuille flow.** In section 2.2, we considered the possibility of Poiseuille flow inlet conditions. Here, the leading-order axial velocity has radial dependence and is incompatible with the leading-order Trouton flow profile. A different boundary-layer analysis is required to account for this, and indeed for any inlet condition where the axial velocity has radial dependence at leading order. In particular, the axial velocity would need to change by an  $O(1)$  amount in the bulk, and this in turn would require that the radial velocity is an order of magnitude larger, and the appropriate scalings would be

$$(7.1) \quad z = \epsilon \tilde{z}, \quad w = \epsilon^{-1} \tilde{w}, \quad p = \epsilon^{-1} \tilde{p}.$$

In this scenario the increased radial velocity may induce an  $O(1)$  change in the fiber radius. By conservation of mass, this would mean that the uniform axial velocity as the fiber exits the boundary layer would take a value other than 1. As such, the leading-order solution may change quantitatively. However, it seems reasonable to anticipate that the appropriate asymptotic expansion will proceed in powers of  $\epsilon$ , as it does for the problem considered here. Again, this scenario may warrant further investigation in the future.

**8. Temperature effects.** In drawing processes, the viscosity of the viscous fluid may vary significantly due to changes in temperature (see, e.g., [28, 29]). In the simplest cases, heat transfer to the fluid is strong so that the temperature (and hence viscosity) can be treated as functions of  $z$  only, which are not coupled to the flow profile. The corresponding governing equations and approximate asymptotic solution for a small aspect ratio are modified only slightly provided the change in viscosity is not too extreme, as outlined in Appendix A.

Elsewhere in the literature, in [23] a fiber drawing model is presented with a two-way coupling between temperature and velocity. The authors consider the parameter regime  $\epsilon \text{Pe} / \text{Bi} = 1$ , where  $\text{Pe}$  is the Péclet number,  $\text{Bi}$  is the Biot number, and the temperature varies across the fiber radius at leading order. Making an ad hoc assumption of a parabolic temperature profile allows the leading-order velocity to be described in terms of an averaged temperature, and a correction associated with the leading-order radial dependence of the viscosity is then computed. Although the role of radially varying temperature appears to be resolved accurately, the mathematical derivation has some shortcomings: the assumed temperature profile does not



satisfy the heat equation, and the velocity is expanded in powers of  $\epsilon$  but the fiber radius and temperature are not, so the contributions associated with these are not included.

**9. Discussion.** In this paper we analyze a mathematical model for fiber drawing based on the assumption that the aspect ratio  $\epsilon \rightarrow 0$ . Our central result is that corrections to the leading-order Trouton model are different for different boundary conditions, are different from those previously reported in the literature for the boundary conditions considered here, and scale linearly with  $\epsilon$  in the case of applied velocity conditions. We calculated these corrections using a combination of boundary-layer analysis and numerical methods and hence derived composite solutions accurate to  $O(\epsilon^2)$ , as well as the correct axial tension required to attain a particular draw ratio.

The asymptotic structure can be summarized as follows. The leading-order axial velocity does not vary radially, and it increases exponentially between its inlet and outlet values. The radial velocity is an order of magnitude smaller and at leading order is linear in  $r$ : this is incompatible with boundary conditions that include zero radial velocity, and so the velocity profile in the fiber must adjust to its bulk profile over boundary layers near the inlet and outlet whose size scales with the fiber radius. The dynamics in the boundary layers can be described by a single canonical system of partial differential equations, independent of both aspect ratio  $\epsilon$  and draw ratio  $D$ . The matching conditions for the bulk for any system can then be determined by an appropriate rescaling. These matching conditions necessitate the introduction of  $O(\epsilon)$  corrections to the bulk flow. This result demonstrates that simply applying averaged boundary conditions to averaged bulk quantities leads to the loss of important information about the fiber dynamics. The  $O(\epsilon)$  corrections are in excellent agreement with numerical solutions to the full axisymmetric fiber description. If stress boundary conditions are applied instead of the velocity conditions considered in the main part of the paper, then the corrections to the leading-order description are  $O(\epsilon^2)$ , but a boundary-layer analysis is still required to determine the correct boundary conditions for the  $O(\epsilon^2)$  equations.

The requirement for boundary-layer analysis and  $O(\epsilon)$  correction terms is not unique to the scenario studied here. An analogous asymptotic structure and calculation of corrections was presented in [21] for drawing of a viscous sheet. The occurrence of this phenomenon across multiple geometries suggests the existence of a ubiquitous phenomenon whereby any extensional flow profile has two-dimensional boundary layers where the flow profile adjusts to its one-dimensional bulk profile. Beyond Newtonian fluids, long and slender sheets and fibers exist in a plethora of other real-world scenarios. For cereal extrusion, the difference between numerics and the leading-order long-and-thin solution for extrusion of a compressible fluid was found to scale linearly with aspect ratio as opposed to quadratically in [19], although the corresponding boundary layer has not yet been analyzed. Viscoelastic fluids are also common in drawing and spinning, and the boundary-layer structure outlined here may be useful for giving insight into aspects of these processes such as die swell, whereby the fiber radius increases directly below the inlet before subsequently decreasing [1, 3]. Finally, this approach could also prove useful for scenarios involving plastic flow, such as metal sheet rolling [2].

## Appendix A. Analysis for axially varying viscosity.

**A.1. Dimensionless model.** Here we consider an axially varying viscosity. We scale the dimensional viscosity with a typical value  $\mu^*$  and define a dimensionless

viscosity  $\mu = \mu(z)$ . The dimensionless governing equations (2.12)–(2.19) in this case are as follows. In the bulk,

$$(A.1) \quad \frac{1}{r} \frac{\partial}{\partial r} (ru) + \frac{\partial w}{\partial z} = 0,$$

$$(A.2) \quad \frac{1}{r} \frac{\partial}{\partial r} \left[ r \left( -p + 2\mu \frac{\partial u}{\partial r} \right) \right] - \frac{1}{r} \left( -p + 2\mu \frac{u}{r} \right) + \frac{\partial}{\partial z} \left( \mu \frac{\partial w}{\partial r} + \epsilon^2 \mu \frac{\partial u}{\partial z} \right) = 0,$$

$$(A.3) \quad \frac{1}{r} \frac{\partial}{\partial r} \left[ r \left( \epsilon^{-2} \mu \frac{\partial w}{\partial r} + \mu \frac{\partial u}{\partial z} \right) \right] + \frac{\partial}{\partial z} \left( -p + 2\mu \frac{\partial w}{\partial z} \right) = 0.$$

At the free boundary  $r = R(z)$ ,

$$(A.4) \quad u = \frac{dR}{dz} w,$$

$$(A.5) \quad -p + 2\mu \frac{\partial u}{\partial r} = \frac{dR}{dz} \left( \mu \frac{\partial w}{\partial r} + \epsilon^2 \mu \frac{\partial u}{\partial z} \right),$$

$$(A.6) \quad \epsilon^{-2} \mu \frac{\partial w}{\partial r} + \mu \frac{\partial u}{\partial z} = \frac{dR}{dz} \left( -p + 2\mu \frac{\partial w}{\partial z} \right),$$

and at the inlet and outlet

$$(A.7) \quad w = 1, \quad u = 0, \quad R = 1 \text{ at } z = 0,$$

$$(A.8) \quad w = D, \quad u = 0 \quad \text{at } z = 1.$$

The cross-averaged mass and momentum equations are

$$(A.9) \quad \frac{d}{dz} \int_0^{R(z)} rw \, dr = 0,$$

$$(A.10) \quad \frac{d}{dz} \int_0^{R(z)} r \left[ -p + 2\mu \frac{\partial w}{\partial z} \right] dr = 0.$$

**A.2. Bulk equations.** Repeating the analysis of section 4.1, the  $O(1)$  quantities obey

$$(A.11) \quad w_0 = W_0(z), \quad u_0 = -\frac{r}{2} W'_0(z), \quad p_0 = -\mu W'_0(z),$$

$$(A.12) \quad \frac{d}{dz} (R_0^2 W_0) = 0, \quad \frac{d}{dz} (3\mu R_0^2 W'_0) = 0,$$

$$(A.12) \quad W_0(0) = 1, \quad R_0(0) = 1, \quad W_1(1) = D,$$

and thus are given by

$$(A.14) \quad w_0 = D^Z,$$

$$(A.15) \quad R_0 = D^{-Z/2},$$

$$(A.16) \quad u_0 = -\frac{r \ln(D)}{2} \frac{1}{M \mu(z)} D^Z,$$

$$(A.17) \quad p_0 = -\frac{\ln(D)}{M} D^Z,$$

where

$$(A.18) \quad Z(z) = \frac{1}{M} \int_0^z \frac{1}{\mu(z')} \, dz' \in [0, 1]$$

is a modified axial variable, with  $M = \int_0^1 \frac{1}{\mu(z')} \, dz'$ .

Meanwhile, the  $O(\epsilon)$  quantities obey

$$(A.19) \quad w_1 = W_1(z), \quad u_1 = -\frac{r}{2} W'_1(z), \quad p_1 = -\mu W'_1(z),$$

$$(A.20) \quad \frac{d}{dz} (R_0^2 W_1 + 2R_0 R_1 W_0) = 0, \quad \frac{d}{dz} [3\mu (R_0^2 W'_1 + 2R_0 R_1 W'_0)] = 0,$$

and, as in sections 5 and 6, the description of the  $O(\epsilon)$  corrections must be completed by considering boundary layers near the inlet and outlet.

**A.3. Boundary layer analysis.** We resolve the boundary layers near the inlet and outlet via the rescalings

$$(A.21a) \quad z = \epsilon \bar{z}, \quad r = \bar{r},$$

and

$$(A.21b) \quad z = 1 - \epsilon D^{-1/2} \bar{z}, \quad r = D^{-1/2} \bar{r},$$

respectively. We assume that the viscosity varies on the global axial lengthscale in the bulk of the domain, but we account for the possibility that it may also vary inside of the boundary layers by defining

$$(A.22) \quad \bar{\mu}(\bar{z}) = \mu(z).$$

The modified axial coordinate  $Z$  should also be rescaled near the inlet and outlet via

$$(A.23a) \quad Z(0 + \epsilon \bar{z}) = \frac{\epsilon}{M} \int_0^{\bar{z}} \frac{1}{\bar{\mu}(\bar{z}')} \, d\bar{z}' = \frac{\epsilon}{M} \bar{Z}$$

and

$$(A.23b) \quad Z(1 - \epsilon D^{-1/2} \bar{z}) = \frac{1}{M} \int_0^1 \frac{1}{\mu} \, dz - \frac{\epsilon D^{-1/2}}{M} \int_0^{\bar{z}} \frac{1}{\bar{\mu}(\bar{z}')} \, d\bar{z}' = 1 - \frac{\epsilon D^{-1/2}}{M} \bar{Z},$$

respectively. We note that  $d\bar{Z}/d\bar{z} = 1/\bar{\mu}(\bar{z})$  in both boundary layers.

We can now propose boundary-layer solutions, analogous to those given by (5.2)–(5.5) and (5.15)–(5.18). For simplicity, we use conservation of mass to assume that  $\bar{R}(1) = 1/\sqrt{D}$  and use solutions of the form

$$(A.24) \quad w(r, z) = 1 + \epsilon \frac{\ln(D)}{M} (\bar{Z} + \bar{w}(\bar{r}, \bar{z})) + \cdots,$$

$$(A.25) \quad R(z) = 1 + \epsilon \frac{\ln(D)}{M} \left( -\frac{\bar{Z}}{2} + \bar{R}(\bar{z}) \right) + \cdots,$$

$$(A.26) \quad u(r, z) = \frac{\ln(D)}{M} \left( -\frac{\bar{r}}{2\bar{\mu}} + \bar{u}(\bar{r}, \bar{z}) \right) + \cdots,$$

$$(A.27) \quad p(r, z) = \frac{\ln(D)}{M} (-1 + \bar{p}(\bar{r}, \bar{z})) + \cdots$$

near the inlet and of the form

$$(A.28) \quad w(r, z) = D \left[ 1 - \epsilon D^{-1/2} \frac{\ln(D)}{M} (\bar{Z} + \bar{w}(\bar{r}, \bar{z})) + \dots \right],$$

$$(A.29) \quad R(z) = D^{-1/2} \left[ 1 - \epsilon D^{-1/2} \frac{\ln(D)}{M} \left( -\frac{\bar{Z}}{2} + \bar{R}(\bar{z}) \right) + \dots \right],$$

$$(A.30) \quad u(r, z) = D^{1/2} \frac{\ln(D)}{M} \left( -\frac{\bar{r}}{2\bar{\mu}} + \bar{u}(\bar{r}, \bar{z}) \right) + \dots,$$

$$(A.31) \quad p(r, z) = D \frac{\ln(D)}{M} (-1 + \bar{p}(\bar{r}, \bar{z})) + \dots$$

near the outlet. Substituting these into the governing equations (A.21) yields a system of boundary-layer equations

$$(A.32) \quad \frac{1}{\bar{r}} \frac{\partial}{\partial \bar{r}} (\bar{r} \bar{u}) + \frac{\partial \bar{w}}{\partial \bar{z}} = 0,$$

$$(A.33) \quad \frac{1}{\bar{r}} \frac{\partial}{\partial \bar{r}} \left[ \bar{r} \left( -\bar{p} + 2\bar{\mu} \frac{\partial \bar{u}}{\partial \bar{r}} \right) \right] - \frac{1}{\bar{r}} \left( -\bar{p} + 2\bar{\mu} \frac{\bar{u}}{\bar{r}} \right) + \frac{\partial}{\partial \bar{z}} \left( \bar{\mu} \frac{\partial \bar{w}}{\partial \bar{r}} + \bar{\mu} \frac{\partial \bar{u}}{\partial \bar{z}} \right) = 0,$$

$$(A.34) \quad \frac{1}{\bar{r}} \frac{\partial}{\partial \bar{r}} \left[ \bar{r} \left( \bar{\mu} \frac{\partial \bar{w}}{\partial \bar{r}} + \bar{\mu} \frac{\partial \bar{u}}{\partial \bar{z}} \right) \right] + \frac{\partial}{\partial \bar{z}} \left( -\bar{p} + 2\bar{\mu} \frac{\partial \bar{w}}{\partial \bar{z}} \right) = 0,$$

which are a modification of the canonical free-boundary problem (5.6)–(5.8) for uniform viscosity. The free-boundary conditions (A.22) are now

$$(A.35) \quad \bar{u} = \frac{d\bar{R}}{d\bar{z}} \bar{w},$$

$$(A.36) \quad -\bar{p} + 2\bar{\mu} \frac{\partial \bar{u}}{\partial \bar{r}} = 0,$$

$$(A.37) \quad \bar{\mu} \frac{\partial \bar{w}}{\partial \bar{r}} + \bar{\mu} \frac{\partial \bar{u}}{\partial \bar{z}} = 0$$

at  $\bar{r} = 1$ , which is again a slight modification of the uniform-viscosity case, and the boundary conditions at  $\bar{z} = 0$  are

$$(A.38) \quad \bar{w} = \bar{R} = 0, \quad \bar{u} = \frac{\bar{r}}{2\bar{\mu}}.$$

We anticipate that the far-field values of  $\bar{w}$  and  $\bar{R}$  may be different for different viscosity profiles  $\bar{\mu}(\bar{z})$  and therefore may be different for the inlet and outlet problems, so we introduce corresponding notation

$$(A.39a) \quad \bar{w}(\bar{r}, \bar{z} \rightarrow \infty; \mu^{(\text{in})}) = -2\bar{R}(\bar{z} \rightarrow \infty; \mu^{(\text{in})}) = c_w^{(\text{in})},$$

$$(A.39b) \quad \bar{w}(\bar{r}, \bar{z} \rightarrow \infty; \mu^{(\text{out})}) = -2\bar{r}(\bar{z} \rightarrow \infty; \mu^{(\text{out})}) = c_w^{(\text{out})}.$$

**A.4. Resolving bulk and boundary layers.** Solving the governing equations (A.20) subject to boundary conditions

$$(A.40a) \quad w_1 = c_w^{(\text{in})} \frac{\ln(D)}{M}, \quad R_1(\bar{z} \rightarrow \infty) = -\frac{c_w^{(\text{in})}}{2} \frac{\ln(D)}{M} \quad \text{at } z = 0,$$

$$(A.40b) \quad w_1 = -c_w^{(\text{out})} \sqrt{D} \frac{\ln(D)}{M} \quad \text{at } z = 1$$

yields finally a modified set of corrections

$$(A.41) \quad w_1 = D^Z \frac{\ln(D)}{M} \left[ c_w^{(\text{in})} - \left( c_w^{(\text{in})} + \frac{c_w^{(\text{out})}}{\sqrt{D}} \right) Z \right],$$

$$(A.42) \quad R_1 = -\frac{1}{2} D^{-Z/2} \frac{\ln(D)}{M} \left[ c_w^{(\text{in})} - \left( c_w^{(\text{in})} + \frac{c_w^{(\text{out})}}{\sqrt{D}} \right) Z \right],$$

$$(A.43) \quad u_1 = -\frac{r}{2\mu} \frac{\ln(D)}{M^2} D^Z \left[ \ln(D) c_w^{(\text{in})} - \left( c_w^{(\text{in})} + \frac{c_w^{(\text{out})}}{\sqrt{D}} \right) (1 + \ln(D)Z) \right],$$

$$(A.44) \quad p_1 = -\frac{\ln(D)}{M^2} D^Z \left[ \ln(D) c_w^{(\text{in})} - \left( c_w^{(\text{in})} + \frac{c_w^{(\text{out})}}{\sqrt{D}} \right) (1 + \ln(D)Z) \right].$$

We can thus see that an axially varying viscosity changes the solution quantitatively, but does not change the qualitative behavior and in particular does not affect the boundary layer structure. However, we note that the length of the boundary layer will decrease as  $\mu$  increases, so if  $\mu$  changes by many orders of magnitude and cannot be treated as  $O(1)$ , then this analysis would break down and an alternative approach would be needed. This is relevant in some glass drawing scenarios [20] and so may warrant further investigation in the future.

**Appendix B. Numerical solutions.** It is easier to write the governing equations in weak form if the momentum balance is written in the form  $\nabla \cdot \boldsymbol{\sigma} = \mathbf{0}$  where  $\boldsymbol{\sigma}$  is the stress tensor, i.e.,

$$(B.1a) \quad \frac{1}{r} \frac{\partial}{\partial r} \left[ r \left( -p + 2 \frac{\partial u}{\partial r} \right) \right] - \frac{1}{r} \left( -p + 2 \frac{u}{r} \right) + \frac{\partial}{\partial z} \left( \epsilon^2 \frac{\partial u}{\partial z} + \frac{\partial w}{\partial r} \right) = 0,$$

$$(B.1b) \quad \frac{1}{r} \frac{\partial}{\partial r} \left[ r \left( \frac{\partial u}{\partial z} + \epsilon^{-2} \frac{\partial w}{\partial r} \right) \right] + \frac{\partial}{\partial z} \left( -p + 2 \frac{\partial w}{\partial z} \right) = 0.$$

We map the problem onto a fixed domain by making a change of variables

$$(B.2) \quad \eta = \frac{r}{R(z)}, \quad \zeta = z,$$

so that  $(\eta, \zeta) \in [0, 1] \times [0, 1]$ . We thus rewrite derivatives using the chain rule as

$$(B.3) \quad \frac{\partial}{\partial r} = \frac{1}{R(\zeta)} \frac{\partial}{\partial \eta}, \quad \frac{\partial}{\partial z} = \frac{\partial}{\partial \zeta} - \frac{R'(\zeta)}{R(\zeta)} \eta \frac{\partial}{\partial \eta}.$$

Substituting this change of variables into the mass and momentum equations (2.12) and (B.1a)–(B.1b) yields

$$(B.4a) \quad \frac{1}{R} \frac{1}{\eta} \frac{\partial}{\partial \eta} (\eta u) + \frac{\partial w}{\partial \zeta} - \frac{R'}{R} \eta \frac{\partial w}{\partial \eta} = 0,$$

$$(B.4b) \quad \frac{1}{R} \frac{1}{\eta} \frac{\partial}{\partial \eta} \left[ \eta \left( -p + 2 \frac{1}{R} \frac{\partial u}{\partial \eta} \right) \right] - \frac{1}{R} \frac{1}{\eta} \left( -p + 2 \frac{1}{R} \frac{u}{\eta} \right) + \left( \frac{\partial}{\partial \zeta} - \frac{R'(\zeta)}{R(\zeta)} \eta \frac{\partial}{\partial \eta} \right) \left[ \epsilon^2 \left( \frac{\partial u}{\partial \zeta} - \frac{R'(\zeta)}{R(\zeta)} \eta \frac{\partial u}{\partial \eta} \right) + \frac{1}{R} \frac{\partial w}{\partial \eta} \right] = 0,$$

$$(B.4c) \quad \frac{1}{R} \frac{1}{\eta} \frac{\partial}{\partial \eta} \left[ \eta \left( \frac{\partial u}{\partial \zeta} - \frac{R'(\zeta)}{R(\zeta)} \eta \frac{\partial u}{\partial \eta} + \epsilon^{-2} \frac{1}{R} \frac{\partial w}{\partial \eta} \right) \right] + \left( \frac{\partial}{\partial \zeta} - \frac{R'(\zeta)}{R(\zeta)} \eta \frac{\partial}{\partial \eta} \right) \left[ -p + 2 \left( \frac{\partial w}{\partial \zeta} - \frac{R'(\zeta)}{R(\zeta)} \eta \frac{\partial w}{\partial \eta} \right) \right] = 0.$$

The corresponding free-boundary conditions (2.15)–(2.17) become

$$(B.5) \quad u = R'(\zeta)w,$$

$$(B.6) \quad -p + 2 \frac{1}{R} \frac{\partial u}{\partial \eta} = R'(\zeta) \left[ \frac{1}{R} \frac{\partial w}{\partial \eta} + \epsilon^2 \left( \frac{\partial u}{\partial \zeta} - \frac{R'}{R} \eta \frac{\partial u}{\partial \eta} \right) \right],$$

$$(B.7) \quad \epsilon^{-2} \frac{1}{R} \frac{\partial w}{\partial \eta} + \left( \frac{\partial u}{\partial \zeta} - \frac{R'}{R} \eta \frac{\partial u}{\partial \eta} \right) = R'(z) \left[ -p + 2 \left( \frac{\partial w}{\partial \zeta} - \frac{R'}{R} \eta \frac{\partial w}{\partial \eta} \right) \right],$$

applied now at the fixed boundary  $\eta = 1$ . The inlet and outlet conditions remain unchanged and are

$$(B.8) \quad w = 1, \quad u = 0, \quad R = 1 \text{ at } \zeta = 0,$$

$$(B.9) \quad w = D, \quad u = 0 \quad \text{at } \zeta = 1.$$

We note that  $R(\zeta)$  is a function of one variable only and should, in principle, be solved in a different domain to the other variables. This complication is most simply avoided by treating  $R$  as a function of both  $\zeta$  and  $\eta$ , introducing a governing partial differential equation

$$(B.10) \quad \frac{\partial R}{\partial \eta} = 0$$

in the bulk of the domain, and replacing all instances of  $R'$  with  $\partial R / \partial \zeta$ .

#### REFERENCES

- [1] J. BATCHELOR, J. BERRY, AND F. HORSFALL, *Die swell in elastic and viscous fluids*, Polymer, 14 (1973), pp. 297–299.
- [2] C. CAWTHORN, J. MINTON, AND E. BRAMBLEY, *Asymptotic analysis of cold sandwich rolling*, Int. J. Mech. Sci., 106 (2016), pp. 184–193.
- [3] J. C. CHANG AND M. M. DENN, *An experimental study of isothermal spinning of a Newtonian and viscoelastic liquid*, J. Non-Newton. Fluid Mech., 5 (1979), pp. 369–385.
- [4] L. CUMMINGS AND P. HOWELL, *On the evolution of non-axisymmetric viscous fibres with surface tension, inertia and gravity*, J. Fluid Mech., 389 (1999), pp. 361–389.
- [5] Y. DEMAY AND J.-F. AGASSANT, *An overview of molten polymer drawing instabilities*, Int. Polym. Process., 29 (2014), pp. 128–139.
- [6] J. DEWYNNE, J. OCKENDON, AND P. WILMOTT, *A systematic derivation of the leading-order equations for extensional flows in slender geometries*, J. Fluid Mech., 244 (1992), pp. 323–338.
- [7] R. J. FISHER, M. M. DENN, AND R. I. TANNER, *Initial profile development in melt spinning*, Ind. Eng. Chem. Fundam., 19 (1980), pp. 195–197.
- [8] A. D. FITT, K. FURUSAWA, T. M. MONRO, C. P. PLEASE, AND D. J. RICHARDSON, *The mathematical modelling of capillary drawing for holey fibre manufacture*, J. Engrg. Math., 43 (2002), pp. 201–227.
- [9] G. GEORGIU, L. OLSON, W. SCHULTZ, AND S. SAGAN, *A singular finite element for Stokes flow: The stick-slip problem*, Internat. J. Numer. Methods Fluids, 9 (1989), pp. 1353–1367.
- [10] W. A. GIFFORD, *A finite element analysis of isothermal fiber formation*, Phys. Fluids, 25 (1982), pp. 219–225.
- [11] I. M. GRIFFITHS AND P. D. HOWELL, *The surface-tension-driven evolution of a two-dimensional annular viscous tube*, J. Fluid Mech., 593 (2007), pp. 181–208.

- [12] I. M. GRIFFITHS AND P. D. HOWELL, *Mathematical modelling of non-axisymmetric capillary tube drawing*, J. Fluid Mech., 605 (2008), pp. 181–206.
- [13] I. M. GRIFFITHS AND P. D. HOWELL, *The surface-tension-driven retraction of a viscida*, SIAM J. Appl. Math., 70 (2010), pp. 1453–1487.
- [14] P. HOWELL, *Extensional Thin Layer Flows*, Ph.D. thesis, University of Oxford, 1994.
- [15] J.-C. HYUN, *Draw resonance in polymer processing: A short chronology and a new approach*, Korea-Aust. Rheol. J., 11 (1999), pp. 279–285.
- [16] H. G. LANDAU, *Heat conduction in a melting solid*, Quart. Appl. Math., 8 (1950), pp. 81–94.
- [17] A. LOGG, K.-A. MARDAL, AND G. WELLS, *Automated Solution of Differential Equations by the Finite Element Method: The FEniCS Book*, Lect. Notes Comput. Sci. Eng. 84, Springer Science & Business Media, New York, 2012.
- [18] M. A. MATOVICH AND J. R. A. PEARSON, *Spinning a molten threadline. Steady-state isothermal viscous flows*, Ind. Eng. Chem. Fundam., 8 (1969), pp. 512–520.
- [19] M. MCPHAIL, *Mathematical Modelling of Cereal Extrusion*, Ph.D. thesis, University of Oxford, 2019.
- [20] D. O’KIELY, C. J. W. BREWARD, I. M. GRIFFITHS, P. D. HOWELL, AND U. LANGE, *Edge behaviour in the glass sheet redraw process*, J. Fluid Mech., 785 (2015), pp. 248–269.
- [21] D. O’KIELY, C. J. W. BREWARD, I. M. GRIFFITHS, P. D. HOWELL, AND U. LANGE, *Glass sheet redraw through a long heater zone*, IMA J. Appl. Math., 83 (2018), pp. 799–820.
- [22] D. O’KIELY, C. J. W. BREWARD, I. M. GRIFFITHS, P. D. HOWELL, AND U. LANGE, *Out-of-plane buckling in two-dimensional glass drawing*, J. Fluid Mech., 869 (2019), pp. 587–609.
- [23] A. G. PAGE, M. BECHERT, F. GALLAIRE, AND F. SORIN, *Unraveling radial dependency effects in fiber thermal drawing*, Appl. Phys. Lett., 115 (2019), 044102.
- [24] J. R. A. PEARSON AND M. A. MATOVICH, *Spinning a molten threadline. Stability*, Ind. Eng. Chem. Fundam., 8 (1969), pp. 605–609.
- [25] C. J. S. PETRIE AND M. M. DENN, *Instabilities in polymer processing*, AIChE J., 22 (1976), pp. 209–236.
- [26] B. SCHEID, S. QUILIGOTTI, B. TRAN, R. GY, AND H. STONE, *On the (de)stabilization of draw resonance due to cooling*, J. Fluid Mech., 636 (2009), pp. 155–176.
- [27] W. W. SCHULTZ AND S. H. DAVIS, *One-dimensional liquid fibers*, J. Rheol., 26 (1982), pp. 331–345.
- [28] Y. STOKES, J. WYLIE, AND M. CHEN, *Coupled fluid and energy flow in fabrication of microstructured optical fibres*, J. Fluid Mech., 874 (2019), pp. 548–572.
- [29] M. TARONI, C. J. W. BREWARD, L. J. CUMMINGS, AND I. M. GRIFFITHS, *Asymptotic solutions of glass temperature profiles during steady optical fibre drawing*, J. Engrg. Math., 80 (2013), pp. 1–20.
- [30] A. TOKAREV, O. TROTSSENKO, I. GRIFFITHS, H. STONE, AND S. MINKO, *Magnet spinning of nano- and microfibers*, Adv. Mater., 27 (2015), pp. 3560–3565.
- [31] F. TROUTON, *On the coefficient of viscous traction and its relation to that of viscosity*, Proc. A, 77 (1906), pp. 426–440.